CrossMark

J. Fluid Mech. (2017), *vol.* 813, R5, doi:10.1017/jfm.2017.15

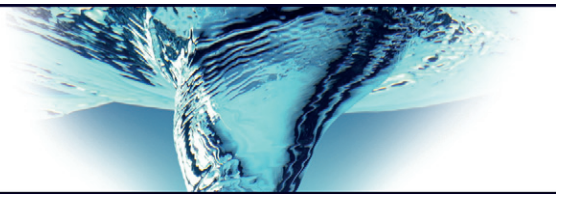

JFM RAPIDS
journals.cambridge.org/rapids

Experimental observation of viscoelastic fluid–structure interactions

Anita A. Dey[1], Yahya Modarres-Sadeghi[1] and Jonathan P. Rothstein[1,†]

[1]Department of Mechanical and Industrial Engineering, University of Massachusetts, Amherst, MA 01003, USA

(Received 4 October 2016; revised 4 January 2017; accepted 5 January 2017; first published online 26 January 2017)

It is well known that when a flexible or flexibly mounted structure is placed perpendicular to the flow of a Newtonian fluid, it can oscillate due to the shedding of separated vortices. Here, we show for the first time that fluid–structure interactions can also be observed when the fluid is viscoelastic. For viscoelastic fluids, a flexible structure can become unstable in the absence of fluid inertia, at infinitesimal Reynolds numbers, due to the onset of a purely elastic flow instability. Nonlinear periodic oscillations of the flexible structure are observed and found to be coupled to the time-dependent growth and decay of viscoelastic stresses in the wake of the structure.

Key words: flow–structure interactions, low-Reynolds-number flows, viscoelasticity

1. Introduction

Several fluid–structure interaction (FSI) studies have been performed with Newtonian fluids. However, to date, no viscoelasticity-induced FSI studies of non-Newtonian fluids have been performed. A fundamental understanding of how these viscoelastic fluids interact with flexible structures has the potential to have a significant influence on a number of very different applications, ranging from polymer processing of composites (Ambrosi & Preziosi 2000) to health care of the inner ear (Takeuchi *et al.* 1990) and biolocomotion (Lauga 2009). When a flexible or flexibly mounted body is placed in a Newtonian flow, the mean and/or fluctuating flow forces that act on the structure can drive the motion of the structure. Several phenomena such as vortex-induced vibration, wake-induced vibration, galloping and flutter, to name a few, can be observed in such systems. These phenomena have been studied extensively in recent decades and have been collected in the form of several books and review papers (e.g. Bearman 1984; Blevins 1990; Païdoussis 1998, 2004; Sarpkaya 2004; Williamson & Govardhan 2004; Païdoussis, Price & de Langre 2011). If the same flexible or flexibly mounted structure is placed in a non-Newtonian flow, however, the response

† Email address for correspondence: rothstein@ecs.umass.edu

© Cambridge University Press 2017

https://doi.org/10.1017/jfm.2017.15 Published online by Cambridge University Press

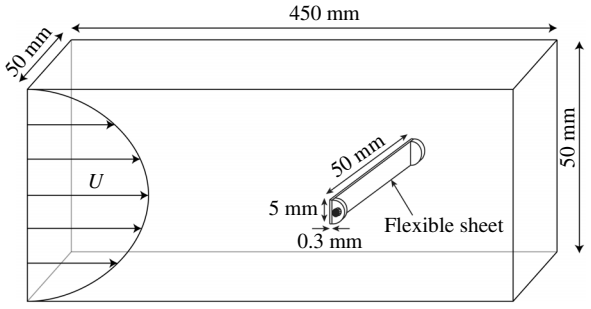

FIGURE 1. Schematic diagram of the set-up.

of the structure is unknown. Unlike Newtonian fluids, the flow of viscoelastic fluids can become unstable at infinitesimal Reynolds numbers in the absence of nonlinear effects of fluid inertia. For non-Newtonian flows, the combination of streamline curvature and fluid elasticity has been found to lead to purely elastic flow instabilities in a host of different flow geometries (Larson 1992; McKinley, Pakdel & Öztekin 1996; Shaqfeh 1996; Groisman & Steinberg 2000). In the present work, we show how the fluctuating flow forces resulting from this purely elastic fluid instability interact with a neighbouring flexible structure.

2. Experimental set-up

In order to observe viscoelastic FSI, a thin flexible rubber sheet was mounted within a rectangular flow cell and exposed to a cross-flow of a viscoelastic wormlike micelle solution. The flow cell was made of acrylic so that it would be transparent and had an internal cross-section of 50 mm $\times$ 50 mm and a length of 450 mm. A positive displacement pump controlled by a linear motor was used to drive the fluid. As shown by Moss & Rothstein (2010), this resulted in minimal pressure and velocity fluctuations. The flow cell was designed to ensure that the flow had a fully developed velocity and elastic stress profile before it reached the flexible sheet. The flow velocity was calculated from the known values of the piston displacement rate and the cross-sectional area of the piston and the flow cell. The thin flexible rectangular sheet was made from natural rubber with an elastic modulus of $E = 101$ kPa and a length of 50 mm, width of 5 mm and thickness of 0.3 mm. The flexible sheet was pinned at its two ends to the walls by gluing it to the flattened ends of two nylon screws inserted through and subsequently flush-mounted to the sidewalls of the flow cell so that they did not protrude into the flow, as shown schematically in figure 1. The sheet was placed at the centre of the rectangular channel and aligned perpendicular to the flow direction. The natural frequency of the sheet was measured to be $f_N = 0.15$ Hz from pluck tests of the mounted sheet in air. The tension in the flexible sheet was maintained by using a sheet length equal to the flow cell width. The viscoelastic wormlike micelle solution used here was composed of 50 mM of the cationic surfactant cetyltrimethyl ammonium bromide (CTAB) and 25 mM of sodium salicylate (NaSal) in deionized distilled water.

A complete set of steady and dynamic shear rheology as well as transient extensional rheology data for this wormlike micelle solution exists (Rothstein 2003). The linear viscoelastic response of this and other wormlike micelle solutions is well fitted by the predictions of a single-mode Maxwell fluid (Rothstein 2003). The

https://doi.org/10.1017/jfm.2017.15 Published online by Cambridge University Press

solution used here has a zero-shear-rate viscosity of $\eta_0 = 200$ Pa s, a relaxation time of $\lambda = 48$ s and is heavily shear thinning, indicating the possible onset of shear banding, although no evidence of shear banding was observed in any of the experiments we discuss later. Filament stretching extensional rheology (FiSER) measurements performed on this solution showed a strong strain hardening of the extensional viscosity, $\eta_E \gg \eta$, for extension rates, $\dot{\xi}$, at which the Weissenberg number, $Wi = \lambda\dot{\xi}$, is greater than one, $Wi > 1$. The Weissenberg number is a measure of the relative importance of elastic to viscous stresses in a flow. For the fluid used here, an extensional viscosity of $\eta_{ext} = 1000$ Pa s, which corresponds to a Trouton ratio of $Tr = \eta_E/\eta_{shear} = 14\,000$, was measured at a Weissenberg number of $Wi = 370$. At similar shear rates, the ratio of the first normal stress to the shear stress was found to be $N_1/\tau = 10$, demonstrating the importance of extensional rheology in this complex flow. In filament stretching experiments (Rothstein 2003; Bhardwaj, Miller & Rothstein 2007), micelle solutions were found to undergo an elastic flow instability during the stretch which resulted in rupture of the fluid filament near its axial midplane. It was hypothesized that the observed filament failure was the result of a breakdown of the wormlike micelles under a large tensile stress (Rothstein 2003). This hypothesis was recently confirmed through molecular dynamics simulations of wormlike micelles under extensional flows (Dhakal & Sureshkumar 2016). For this micelle solution, extensional rheology measurements showed that a maximum tensile stress of $\tau_{rupt} = 7$ kPa could be supported by the filament before the stretched and deformed micelles in the solution would fail. The dynamics of the filament rupture are presented in Bhardwaj *et al.* (2007). A breakdown of wormlike micelle solutions in homogeneous extensional flows similar to that developed during filament stretching has also been shown to lead to elastic flow instabilities in complex flows containing regions of both shear and extensional flows. Examples include the flow past a falling sphere and the flow past one or more circular cylinders. In each case, a strong extensional flow was shown through velocity profile measurements to develop in the wake downstream of the immersed object (Jayaraman & Belmonte 2003; Chen & Rothstein 2004; Handzy & Belmonte 2004; Gladden & Belmonte 2007; Moss & Rothstein 2010; Mohammadigoushki & Muller 2016). In these experiments, once the flow strength was increased to the point where the micelles were stretched beyond their maximum tensile strength, a time-dependent periodic breakdown and recovery of the wormlike micelles in the wake of the immersed object was found to develop even in the absence of fluid inertia. In this paper, we will show that these elastic flow instabilities can have a significant effect on flow past a flexible structure, resulting in the first recorded example of viscoelastic FSI.

The response of the flexible sheet under cross-flow was recorded using a high-speed camera (Phantom V4.2) at 100 frames s^{-1} with a resolution of 144 pixels $\times$ 304 pixels, and the time history of the sheet displacement was obtained using image tracking software (Tracker). Here, we will only present data for the midsection deflection, as measurements across the flexible sheet were all found to be in phase and at the same oscillation frequency. Full-field flow-induced birefringence (FIB) measurements were made to qualitatively visualize the state of viscoelastic stress within the flowing wormlike micelle solution (Fuller 1995; Moss & Rothstein 2010). For the FIB measurements, linear polarizers were installed before and after the flow cell at 45° and 135° to the flow direction and backlit using a white light. In this orientation, micelle deformation/stress in the flow direction becomes visible, thereby emphasizing areas of extensional stress in the wake of the flexible sheet. Using the stress-optical rule, the intensity of the birefringence signal can be converted directly to the stress in the fluid (Fuller 1995).

https://doi.org/10.1017/jfm.2017.15 Published online by Cambridge University Press

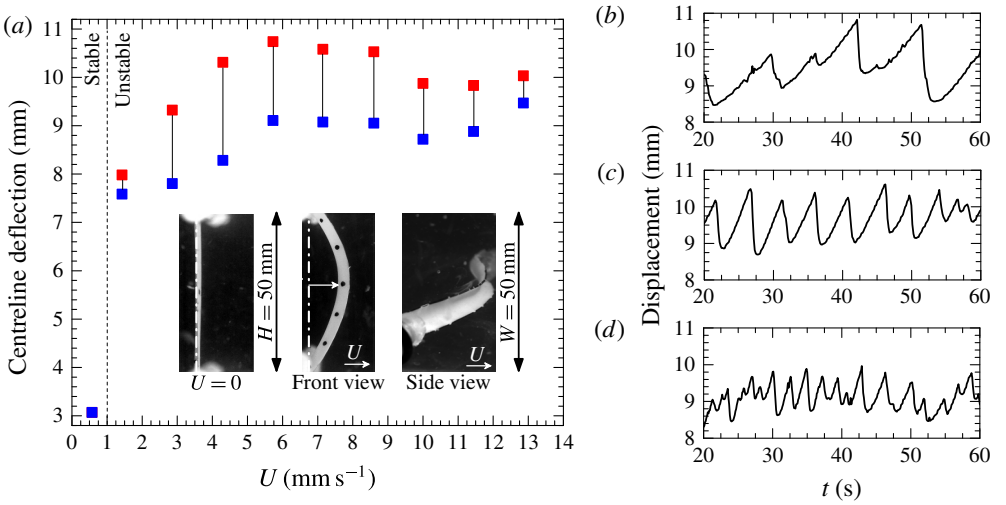

FIGURE 2. The centreline deflection of the flexible sheet versus the flow velocity (*a*), and the time histories of the centreline deflection of the sheet at (*b*) $U = 4.3$ mm s^{-1}, (*c*) $U = 7.15$ mm s^{-1} and (*d*) $U = 11.44$ mm s^{-1}. The critical onset condition, $U = 1.4$ mm s^{-1}, corresponds to $Wi_{crit} = 13$.

3. Results and discussion

3.1. *A flexible sheet perpendicular to the flow*

A series of measurements were made over a range of Reynolds numbers up to $Re = 3.5 \times 10^{-4}$ (defined as $Re = \rho U w/\eta_0$, where ρ is the density of the fluid, U is the flow velocity, w is the width of the sheet and η_0 is the zero-shear-rate viscosity). As a result, these experiments were in the Stokes flow regime and the inertial flow effects could be neglected. At zero flow velocity, the sheet was undisturbed and was aligned perpendicular to the flow direction, as seen in figure 2(*a*). As the cross-flow was applied, the sheet was bent in the flow direction (second and third images in figure 2*a*). It should be noted that in addition to the induced curvature along the length of the sheet that can be observed from the front view in figure 2(*a*), the low flexural rigidity of the sheet resulted in a secondary curvature across the sheet that can be observed from the side view in figure 2(*a*). The resulting cross-sectional profile was 'C' shaped. At low flow velocities, where the Weissenberg number was small, the flow of the wormlike micelle solution remained stable and the static deflection of the sheet grew with increasing flow velocity. As the flow velocity was increased beyond a critical velocity and a corresponding critical Weissenberg number ($Wi_{crit} = 13$), the flow of the wormlike micelle solution became unstable, with periodic fluctuations in the velocity and stress fields around the sheet, observed by tracking particle motion and FIB in the fluid. As was the case for the flow of wormlike micelle solutions past circular cylinders and spheres (Chen & Rothstein 2004; Moss & Rothstein 2010; Mohammadigoushki & Muller 2016), the flow instability originated as a slow growth and fast decay of extensional stress in the wake of the flexible sheet. This can be observed in figure 3 from the time-dependent extension and retraction of the birefringent tail in the wake of the sheet.

The FIB measurements in figure 3 were taken through crossed polarizers to emphasize the intensity of the elastic extensional stress in the fluid. It is difficult

https://doi.org/10.1017/jfm.2017.15 Published online by Cambridge University Press

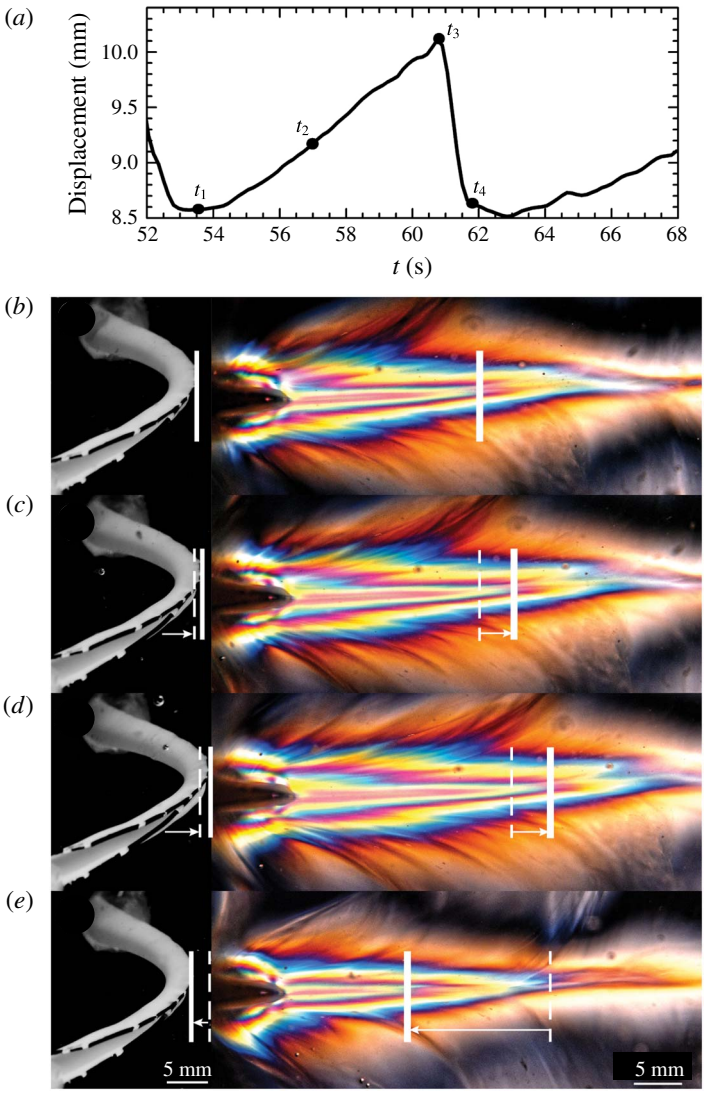

FIGURE 3. Time history of the centreline deflection of the sheet for one period of oscillation (*a*), together with bright-field images of the deformed sheet (left) and the extensional birefringent patterns (right) at $U = 4.3$ mm s^{-1} and for (*b*) $t_1 = 0$, (*c*) $t_2 = 3.45$ s, (*d*) $t_3 = 7.2$ s and (*e*) $t_4 = 7.95$ s. The dashed lines highlight the change in the birefringence patterns and deformations of the sheet between each time interval. The FIB images are viewed perpendicular to the flow direction, while the real bright-field images are taken from an angle to the flow direction in order to show the entire length of the flexible sheet.

to deconvolute these FIB measurements directly into a quantitative value of the viscoelastic stress in the fluid for a number of reasons. Flow-induced birefringence is a line-of-sight technique, which integrates the birefringence contribution from all fluid elements along the light path. Because the flow is three-dimensional, it is not possible to accurately use these FIB measurements to determine the stress.

https://doi.org/10.1017/jfm.2017.15 Published online by Cambridge University Press

Additionally, at these birefringence levels, the stress-optical rule has been shown to break down for this fluid (Rothstein 2003), and any stresses calculated using it would dramatically underpredict the true state of stress in the fluid. The FIB measurements are still a valuable tool for qualitatively observing the growth in the viscoelastic stress and its time-dependent fluctuations. As seen in figure 3, a narrow region of micelle deformation, known as a birefringent tail, formed in the strong extensional flow region just downstream of the stagnation point. In the wake, the fluid must accelerate from rest along the trailing edge of the sheet to the maximum flow velocity, U_{max}, over a short distance downstream of the flexible sheet. This extensional flow resulted in strong micelle alignment and deformation, as seen in figure 3(*b*). As the flow velocity was increased, a stable birefringent tail grew both in length and intensity until the onset of the viscoelastic flow instability. After the onset of the flow instability, the maximum extent of the birefringent tail approached an asymptotic limit. A series of dashed lines have been added to figure 3 to graphically illustrate the magnitude and direction of the changes to the birefringence pattern with time during one oscillation cycle. These lines are placed in the wake of the sheet at a location corresponding to a fixed value of the FIB or elastic stress in the fluid. A similar set of lines have been added to show the deflection of the sheet in the bright-field images to the left of the FIB. At the start of an oscillation (figure 3*b*), the wormlike micelle solution already exhibited a significant amount of elastic stress in the wake. The birefringent tail in the fluid grew in length and intensity with time (figure 3*c*), resulting in still further stretching of the flexible sheet. At its maximum extent (figure 3*d*), the birefringence grew by approximately 30 % beyond its minimum extent (figure 3*b*) to nearly 10w downstream, while the deflection of the sheet increased by roughly 12 % from 8.5 mm to 10 mm. When the displacement of the sheet reached 10 mm, an abrupt breakdown of the wormlike micelles in the high-stress wake was observed, resulting in a rapid loss of elastic stress in the wake. This can be seen in figure 3(*e*) as a significant reduction in the length and extent of the birefringent tail in the fluid. The next oscillatory cycle begins with the flow of fresh unruptured wormlike micelles from upstream of the flexible sheet into its wake, where with time, elastic stress is once again built up in the fluid in the wake of the sheet as the sheet is stretched and deformed back towards its maximum deformation. The result of the cyclical tensile loading and failure of the viscoelastic fluid is the observed periodic motion of the flexible sheet. Similar time-dependent FIB patterns were observed at all flow velocities where the flow of wormlike micelle solution became unstable.

The presence of this viscoelastic flow instability caused the flexible sheet to oscillate around a mean stretched position. As seen in figure 3, the stress growth/decay and the sheet deflection were directly correlated. For this fluid and sheet, the critical velocity for the onset of oscillations was found to be $U_{crit} = 1.4$ mm s^{-1} (figure 2*a*), corresponding to a critical Weissenberg number of $Wi_{crit} = 13$. Unlike several cases of inertia-driven flow-induced instabilities of flexible structures (e.g. vortex induced vibrations (VIV) of a flexible (Bourguet *et al.* 2011) or a flexibly mounted structure (Williamson & Govardhan 2004), or the response of a flexible cylinder in axial flow (Païdoussis 2004; Modarres-Sadeghi *et al.* 2011)), the displacement of the sheet over time was not sinusoidal. The saw-toothed pattern of the time histories (figure 2*b–d*) shows that these oscillations were highly nonlinear. At a cross-flow velocity of $U = 4.3$ mm s^{-1} (figure 2*b*), the structure was found to oscillate with a dominant frequency of $f = 0.11$ Hz. Under these flow conditions, the flexible sheet stretched slowly at a rate of 0.17 mm s^{-1} until a critical breakdown of the wormlike micelles, and the subsequent loss of the viscoelastic stress in the wake of the sheet caused the

https://doi.org/10.1017/jfm.2017.15 Published online by Cambridge University Press

flexible sheet to recoil abruptly. The recoil rate was found to be considerably faster at 1.5 mm s^{-1}. As the flow velocity was increased to $U = 7.15$ mm s^{-1} (figure 2*c*), the frequency of oscillations increased to $f = 0.2$ Hz. The frequency of the flexible sheet oscillations increased roughly linearly with increasing flow rate, seen later in figure 6(*c*). As will be discussed in further detail later, this increase in the overall frequency of oscillations was accompanied by an increase in both the deformation rate of the sheet during the growth phase of the deformation cycle and a slightly slower increase in the recoil rate of the sheet during the decay phase of the deformation cycle. These rates will be presented as a function of flow velocity, alongside a plot of their relative magnitude, later in figure 7. At velocities of $U = 11.44$ mm s^{-1} and beyond, higher harmonics began to emerge in the oscillations of the flexible sheet. These can be observed in figure 2(*d*) and are quite clear from the fast Fourier transform analysis of the data (not shown).

The maximum and minimum deformations of the flexible sheet versus the flow velocity are shown in figure 2(*a*). For each time history, a minimum of 10 cycles and 180 s of data were used. Below $U_{crit} = 1.4$ mm s^{-1}, the flow was stable and the structure underwent a static deflection but did not oscillate. Above U_{crit}, a periodic response was observed. Just beyond this point, the maximum displacement of the flexible sheet increased linearly with the flow velocity until a velocity of $U = 6$ mm s^{-1}, beyond which the maximum sheet deflection reached a plateau and remained more or less unchanged for all flow velocities tested. On the other hand, the amplitude of the sheet oscillations increased linearly until it reached a maximum at $U = 4$ mm s^{-1}. Thereafter, with increasing flow velocity, the oscillation amplitude began to decay.

Two observations can be gleamed from figure 2. First, there are two types of sheet deformation: one is the in-flow bending and stretching of the sheet span and the other is the bending of the cross-section of the sheet into a semicircular 'C'. A simplified diagram of these two types of flexible sheet deformation is shown in figure 4. During the experiments, the flexible sheet deformation remained within the material's elastic limits. Therefore, the stress needed for the cross-flow bending of the sheet from a straight profile into a 'C' profile can be approximated from Hooke's law, $\sigma_{cross\text{-}flow} = E\epsilon$, where $\sigma_{cross\text{-}flow}$ is the bending stress at a layer above/below the neutral axis, $E = 101$ kPa is the known elastic modulus of the flexible sheet and ϵ is the strain, which is the ratio of the distance from the neutral axis and the radius of curvature to the neutral surface. The result is a maximum bending stress of approximately 8 kPa. The stress needed for the in-line bending of the sheet span length to the maximum deflection seen in figure 2(*a*) was calculated using beam theory (Beer *et al.* 2014). The force acting on the sheet was approximated by using the equation of a simply supported beam, $p = -384EIy_{max}/5L^4$, where p is the force per unit length acting on the sheet, E is the elastic modulus, $I = 0.4$ mm^4 is the moment of inertia for the deformed shape as a C-channel, y_{max} is the maximum deflection measured from figure 2(*a*) and L is the flexible sheet length. The resulting in-line bending stress, $\sigma_{inline} = p/w$, where w is the sheet's width, was found to be significantly smaller, in the range of only 10 Pa. In addition to bending, there is a tensile stress which results from the sheet stretching from its initial undeformed state to its deformed elongated contour length at maximum deflection. By calculating the strain, ϵ, from the images of the deformed sheets, this stress was found to be approximately $\sigma_{tensile} = E\epsilon = 13$ kPa. From filament stretching extensional rheology measurements, the wormlike micelle solution was found to rupture and fail at an extensional stress of 7 kPa. Thus, these calculations appear to confirm that the viscoelastic fluidic stresses needed to deform

https://doi.org/10.1017/jfm.2017.15 Published online by Cambridge University Press

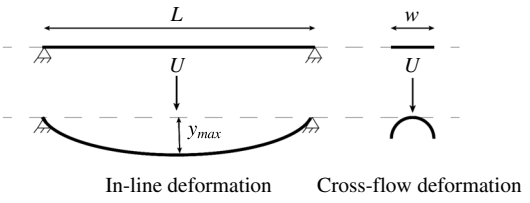

FIGURE 4. A schematic diagram of the in-line and cross-flow deformation of the flexible sheet.

the sheet are large enough to result in breakdown of viscoelastic wormlike micelles in the wake of the sheet, resulting in a time-dependent flow field, which in turn drives the observed time-dependent oscillations of the sheet.

Second, as mentioned before, the deformation rate of the sheet during the oscillations was found to grow linearly with increasing velocity and change more dramatically with increasing flow velocity than the recoil rate. As a result, at low velocities, when the recoil rate was much faster than the growth in the sheet deflection or the deformation rate, the sheet was able to fully recoil before any significant extensional stress could be rebuilt in the micelle solution in the wake of the sheet. As the flow velocity was increased, the deformation and recoil rate of the sheet became more comparable, moving from a 20 : 1 to a 5 : 1 ratio between the deformation and recoil rates, as discussed later. As a result, the sheet was not able to fully recoil before new elastic stresses began building in its wake. At the same time, the breakdown of micelles transitioned from a global to a local phenomenon. The wormlike micelle solution became unstable at multiple isolated locations in the wake of the sheet rather than failing simultaneously across the entire downstream edge. The result was that a complete recoil of the sheet could not be achieved because all of the fluid did not yield simultaneously. Such an instance of local regions of elastic stress in the fluid in the wake along the length of the flexible sheet is illustrated in the time series of FIB images in figure 5. In these images, a patchwork of bright irregular regions of high elastic stress in the fluid was found to fluctuate in space and time during the sheet oscillations observed at a constant flow velocity of $U = 10$ mm s^{-1}. The consequence of these spatial fluctuations was the appearance and growth of higher harmonics in the data and a reduction in the oscillation amplitude with increasing velocity beyond $U = 8$ mm s^{-1}. At lower velocities, the birefringence was found to be constant along the span of the sheet and vary uniformly across the span with the onset of the viscoelastic flow instability and the resulting sheet oscillations. The spatial fluctuations of the FIB within the high-stress regions (figure 5) and the feather-like structures (figure 3) are reminiscent of the Taylor–Gortler vortex structures observed downstream of a circular cylinder in cross-flow of a viscoelastic polymer solution by McKinley, Armstrong & Brown (1993) and Shiang, Özkekin, Lin & Rockwell (2000). In their work, three-dimensional stationary roll cells were observed to be spaced periodically along the axis of the cylinder.

3.2. *Modifying the flexible sheet inclination*

An additional set of experiments was conducted over the same range of Reynolds numbers for cases wherein the flexible sheet was placed at 0°, 20° and 45° to the flow direction. The desired inclination of the flexible sheet was achieved through

https://doi.org/10.1017/jfm.2017.15 Published online by Cambridge University Press

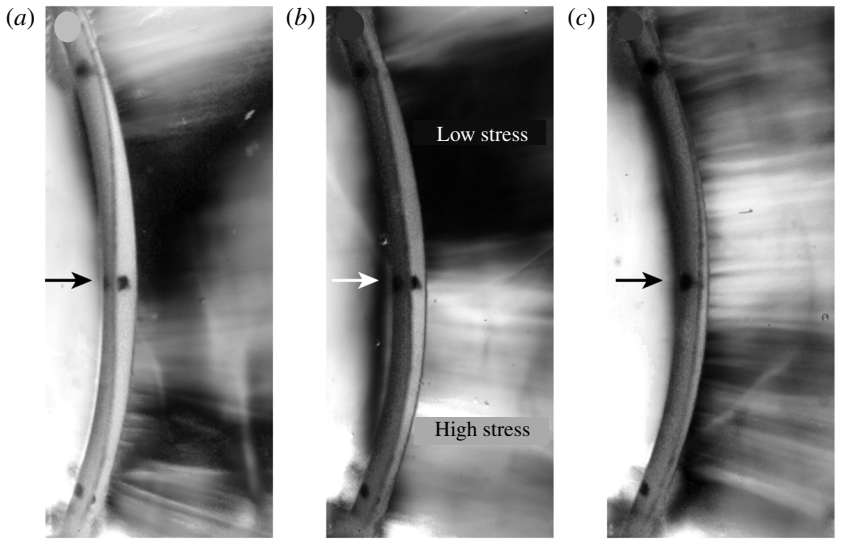

FIGURE 5. Flow-induced birefringence snapshots corresponding to the sequence of fluid rupture in the wake of the flexible sheet for a velocity of $U = 10$ mm s^{-1}. In (*a*), an FIB image is shown at the onset of sheet recoil, time $t = 0$; in (*b*), $t = 0.25$ s, while in (*c*), $t = 0.60$ s, which corresponds to the end of the recoil phase in the oscillation cycle. The bright regions highlight areas of large micelle deformation and large elastic stresses in the fluid, while the darker regions show the locations where the micelles have broken down and the elastic stress in the fluid has been lost.

external rotation of the fixtures holding the flexible sheet inside the flow cell. The 0° orientation did not oscillate for the range of flow rates tested, and, as a result, discussion of the 0° case will not be included in the following. The centreline deflection of the flexible sheet for the three different inclination angles tested is shown in figure 6(*a*). For completeness and ease of comparison, the data for the 90° case have been included in all subsequent figures. The side views of the complex deformation that the flexible sheet underwent for each inclination angle are shown in inset images in figure 6. As the flow began, the 45° flexible sheet was deformed into the flow direction, with its cross-section forming a 'C' shape that was significantly less deformed than that of the 90° case. Unlike the 90° case, the 'C' shape remained open for all of the flow velocities tested and did not completely bend back onto itself. At a critical flow velocity of $U = 2.8$ mm s^{-1}, the wormlike micelle solution became unstable, and periodic oscillations of the flexible sheet started in the same manner as previously observed for the 90° case. The centreline deflection of the 45° flexible sheet increased linearly with flow velocity up to a maximum value that was smaller than that observed for the 90° case. After reaching this maximum value at $U = 5.7$ mm s^{-1}, the centreline deflection decreased and approached a plateau at the higher flow velocities tested. For the 20° inclination, the flexible sheet began from a position aligned almost completely with the flow, and the resulting cross-section profile of the sheet had a much smaller curvature (figure 6*a*). The centreline deflection of the sheet was much smaller than the 45° and 90° cases, with a maximum deflection of 5 mm compared with nearly 11 mm for the 90° case. For flow velocities larger than $U = 4.8$ mm s^{-1}, the 20° flexible sheet did not continue to hold the stretched deformation seen in figure 6(*a*), but instead rotated

https://doi.org/10.1017/jfm.2017.15 Published online by Cambridge University Press

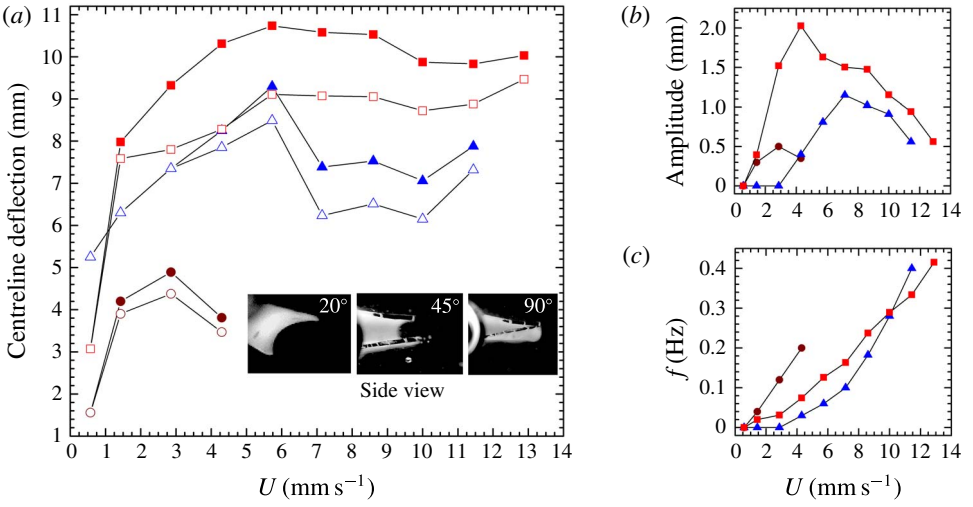

FIGURE 6. (*a*) Centreline displacement of the flexible sheet for 20° (●), 45° (▲) and 90° (■) inclinations. The filled and hollow symbols are used for the maximum and minimum flexible sheet displacements respectively during oscillations at each flow velocity. The insets contain the side views of the cross-flow deformation of the flexible sheet. (*b,c*) Amplitude and frequency of oscillations of the flexible sheet over the range of flow velocities tested. The error margin for the amplitude of oscillations is less than 10 % for flow velocities below 4 mm s^{-1} and less than 5 % for higher flow velocities. The error margin is less than 5 % for the frequency plots.

off the centreline, where it remained in an asymmetric position closer to one of the sidewalls for the rest of the flow velocities tested and exhibited no further large-amplitude fluctuations. Data for the 20° case beyond $U = 4.8$ mm s^{-1} are therefore not presented in figure 6 or any subsequent plots. The amplitude and frequency of oscillations from the centreline deflection time histories are mapped out in figures 6(*b*) and 6(*c*) respectively. The amplitude of oscillations initially increased roughly linearly with increasing flow velocity for all three inclinations tested and reached a maximum. Beyond this maximum, the amplitudes of all three angles began to decay with increasing flow velocity. The oscillation frequency increased with the flow velocity for all three inclinations.

From the sawtooth waveform of the centreline deflection time histories, it was clear that the flexible sheet stretches slowly before recoiling rapidly during each oscillation cycle. In figure 7(*a*), the deformation and recoil velocities of the flexible sheet during oscillations are presented as a function of the flow velocity for all three inclinations. It can be observed that the deformation velocity curve followed a similar trend for all three inclinations over the range of flow velocities tested. The recoil velocities, on the other hand, were very different for the three inclination angles. The 90° inclination curve had the largest recoil velocity by almost a factor of three. This can likely be attributed to the flexible sheet recoil velocity being dependent on the elastic stress built up within the sheet, which is clearly at a maximum within the 90° sheet due to the increased sheet deformation at any given flow velocity. Conversely, the deformation velocity of the sheet is strongly dependent on the flow conditions as it is coupled to the convection of fluid from upstream of the sheet to rebuild elastic stress in the wake of the sheet after a fluid rupture event. As a result, as seen in figure 7(*a*),

https://doi.org/10.1017/jfm.2017.15 Published online by Cambridge University Press

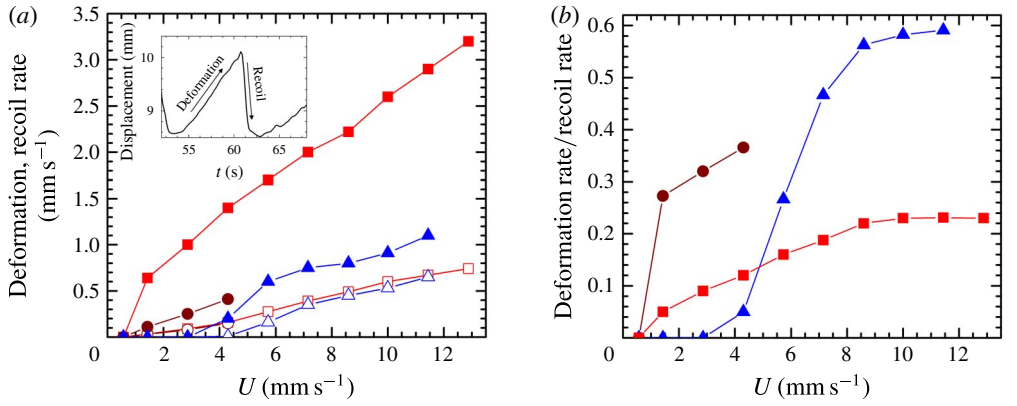

FIGURE 7. (*a*) The deformation rate (open symbols) and recoil rate (filled symbols) during an oscillation cycle for the flexible sheet aligned at a 20° (●), 45° (▲) and 90° (■) inclination to the flow direction as a function of the flow velocity. (*b*) The ratio of deformation and recoil rates of the flexible sheet as a function of the flow velocity for the three flexible sheet inclination angles.

the deformation velocity is not strongly coupled to the sheet orientation. A plot of the ratio of deformation and recoil velocities of the flexible sheet over varying flow velocities is shown in figure 7(*b*). For the 45° and 90° inclination angles, the ratio of the deformation rate to the recoil rate was found to start quite small at a value of less than 0.1 and then to increase with the flow velocity to reach a plateau beyond $U = 8$ mm s^{-1}. This plateau of the ratio of deformation and recoil velocity corresponds to the point at which higher harmonics appear in the oscillations and the amplitude begins to decay. For the case of the 90° sheet, the ratio of deformation rate to recoil rate reached a plateau of just over 0.2. As such, the dynamics of oscillation was dominated by the fast recoil of the sheet after fluid rupture. Conversely, this rate approached 0.6 for the 45° sheet, resulting in a more symmetric oscillation cycle and a growth in deformation that nearly matched its decay. Although the 20° sheet did not reach a plateau before twisting from the centreline, breaking symmetry and ceasing to oscillate, its behaviour appears to be closer to that of the 45° sheet than the 90° sheet.

Finally, we concentrate on the results presented in the previous sections with the objective of combining the dimensional results from the different flexible sheet inclinations into a cohesive set of results using a single non-dimensional parameter. In order to collapse the data for all three inclination angles, a non-dimensional flow velocity, U^*, a non-dimensional oscillation amplitude, A^*, and a non-dimensional frequency, f^*, were considered. The non-dimensional velocity that best collapsed the data in terms of both the critical onset conditions and the flow velocity corresponding to the maximum oscillation amplitude was found to be $U^* = U/(w\sin(\theta)f_\theta)$. Here, U is the flow velocity, w is the width of the flexible sheet, θ is the inclination angle of the sheet, $w\sin(\theta)$ is the equivalent surface area of the flexible sheet exposed to the flow and f_θ is the frequency of oscillations at the critical flow velocity, which depends on the inclination angle of the flexible sheet. As seen in figure 8(*a*), using this dimensionless velocity, both the onset condition and the maximum of the oscillation amplitude collapse to values of $U^* \approx 7$ and $U^* \approx 42$ respectively. It is expected that the appropriate dimensionless velocity should also contain some information about the viscoelastic fluid properties, specifically the relaxation time

https://doi.org/10.1017/jfm.2017.15 Published online by Cambridge University Press

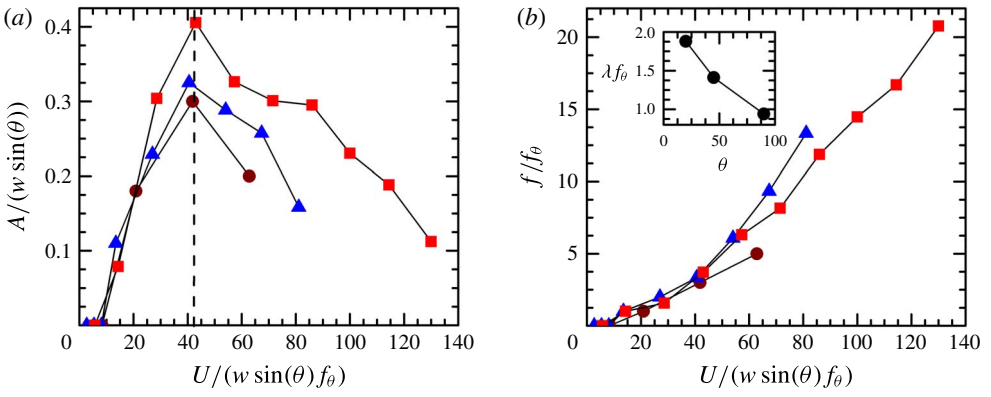

FIGURE 8. The dimensionless (*a*) amplitude and (*b*) frequency of oscillations as a function of the dimensionless flow velocity for flexible sheet inclination angles of 20° (●), 45° (▲) and 90° (■). The inset in (*b*) contains the dimensionless product, λf_θ, as a function of the inclination angle.

of the fluid, λ. However, because in this study only a single fluid composition was used, this hypothesis could not be fully tested. As seen in the inset in figure 8(*b*), a renormalization of the critical oscillation frequency with the relaxation time to form a modified Weissenberg number, $Wi_f = \lambda f_\theta$, appears to be a promising first step towards incorporating rheological information into our analysis as the value approaches $Wi_f \sim 1$. Future studies will focus on how changes in the fluid rheology affect the observed viscoelastic FSI. The appropriate non-dimensional amplitude and frequency were found to be $A^* = A/w\sin(\theta)$ and $f^* = f/f_\theta$, where A and f are the dimensional amplitude and frequency of flexible sheet oscillations respectively. Using these dimensionless parameters, the data from the three inclination angles are collapsed onto a master curve, as seen in figure 8(*a*,*b*). The slight variations in the data are likely the result of the complex deformation of the flexible sheet under flow. The deviation of scaling for higher flow velocities could be due to the higher harmonics that become dominant during oscillations.

4. Conclusion

We have shown, for the very first time, that purely elastic flow instabilities occurring in a viscoelastic fluid flow can drive the motion of a flexible structure placed in its path. The oscillations of the flexible structure, which develop at infinitesimal Reynolds numbers and in the absence of vortex shedding, have been presented for three inclinations of a flexible sheet. The measurements of the structural deformation velocity profiles and the FIB have been used to quantify the time variation of the flow field and the state of stress in the fluid during the oscillations. These results have been further classified using a set of proposed non-dimensional parameters. These observations open up an entirely new field of study. To fully understand this new phenomenon, there are several questions that still need to be answered, including what the role of the structure geometry, modulus, bending stiffness and natural frequency is, how changing fluid properties affect the oscillations, whether this phenomenon is universal to all viscoelastic fluids including polymer solutions and, if so, which dimensionless groups properly describe the physics over this broad space. Many of these studies are ongoing, and we hope to be reporting on them in the near future.

https://doi.org/10.1017/jfm.2017.15 Published online by Cambridge University Press

References

AMBROSI, D. & PREZIOSI, L. 2000 Modeling injection molding processes with deformable porous preforms. *SIAM J. Appl. Maths* **61** (1), 22–42.

BEARMAN, P. W. 1984 Vortex shedding from oscillating bluff bodies. *Annu. Rev. Fluid Mech.* **16** (1), 195–222.

BEER, F. P., JOHNSTON, E. R. JR, DEWOLF, J. T. & MAZUREK, D. 2014 *Mechanics of Materials*. McGraw-Hill Education.

BHARDWAJ, A., MILLER, E. & ROTHSTEIN, J. P. 2007 Filament stretching and capillary breakup extensional rheometry measurements of viscoelastic wormlike micelle solutions. *J. Rheol.* **51** (4), 693–719.

BLEVINS, R. D. 1990 *Flow-Induced Vibration*. Krieger Pub. Co.

BOURGUET, R., MODARRES-SADEGHI, Y., KARNIADAKIS, G. E. & TRIANTAFYLLOU, M. S. 2011 Wake-body resonance of long flexible structures is dominated by counterclockwise orbits. *Phys. Rev. Lett.* **107** (13), 134502.

CHEN, S. & ROTHSTEIN, J. P. 2004 Flow of a wormlike micelle solution past a falling sphere. *J. Non-Newtonian Fluid Mech.* **116** (23), 205–234.

DHAKAL, S. & SURESHKUMAR, R. 2016 Uniaxial extension of surfactant micelles: counterion mediated chain stiffening and a mechanism of rupture by flow-induced energy redistribution. *ACS Macro Lett.* **5**, 108–111.

FULLER, G. G. 1995 *Optical Rheometry of Complex Fluids*. Oxford University Press.

GLADDEN, J. R. & BELMONTE, A. 2007 Motion of a viscoelastic micellar fluid around a cylinder: flow and fracture. *Phys. Rev. Lett.* **98**, 224501.

GROISMAN, A. & STEINBERG, V. 2000 Elastic turbulence in a polymer solution flow. *Nature* **405**, 53–55.

HANDZY, N. Z. & BELMONTE, A. 2004 Oscillatory rise of bubbles in wormlike micellar fluids with different microstructures. *Phys. Rev. Lett.* **92**, 124501.

JAYARAMAN, A. & BELMONTE, A. 2003 Oscillations of a solid sphere falling through a wormlike micellar fluid. *Phys. Rev.* E **67**, 065301.

LARSON, R. 1992 Instabilities in viscoelastic flows. *Rheol. Acta* **31** (3), 213–263.

LAUGA, E. 2009 Life at high Deborah number. *Europhys. Lett.* **86** (6), 64001.

MCKINLEY, G. H., ARMSTRONG, R. C. & BROWN, R. A. 1993 The wake instability in viscoelastic flow past confined circular cylinders. *Phil. Trans. R. Soc. Lond.* A **344** (1671), 265–304.

MCKINLEY, G. H., PAKDEL, P. & ÖZTEKIN, A. 1996 Rheological and geometric scaling of purely elastic flow instabilities. *J. Non-Newtonian Fluid Mech.* **67**, 19–47.

MODARRES-SADEGHI, Y., PAÏDOUSSIS, M., SEMLER, C. & GRINEVICH, E. 2011 Experiments on vertical slender flexible cylinders clamped at both ends and subjected to axial flow. *Phil. Trans. R. Soc. Lond.* A **366**, 1275–1296.

MOHAMMADIGOUSHKI, H. & MULLER, S. J. 2016 Sedimentation of a sphere in wormlike micellar fluids. *J. Rheol.* **60** (4), 587–601.

MOSS, G. R. & ROTHSTEIN, J. P. 2010 Flow of wormlike micelle solutions past a confined circular cylinder. *J. Non-Newtonian Fluid Mech.* **165** (21), 1505–1515.

PAÏDOUSSIS, M. 2004 *Fluid–Structure Interactions: Slender Structures and Axial Flow*, vol. 2. Academic.

PAÏDOUSSIS, M. P. 1998 *Fluid–Structure Interactions: Slender Structures and Axial Flow*, vol. 1. Academic.

PAÏDOUSSIS, M. P., PRICE, S. J. & DE LANGRE, E. 2011 *Fluid–Structure Interactions – Cross-Flow-Induced Instabilities*, vol. 1. Cambridge University Press.

ROTHSTEIN, J. P. 2003 Transient extensional rheology of wormlike micelle solutions. *J. Rheol.* **47** (5), 1227–1247.

SARPKAYA, T. 2004 A critical review of the intrinsic nature of vortex-induced vibrations. *J. Fluids Struct.* **19** (4), 389–447.

SHAQFEH, E. S. G. 1996 Purely elastic instabilities in viscometric flows. *Annu. Rev. Fluid Mech.* **28**, 129–185.

https://doi.org/10.1017/jfm.2017.15 Published online by Cambridge University Press

SHIANG, A. H., ÖZKEKIN, A., LIN, J. C. & ROCKWELL, D. 2000 Hydroelastic instabilities in viscoelastic flow past a cylinder confined in a channel. *Exp. Fluids* **28** (2), 128–142.

TAKEUCHI, K., MAJIMA, Y., HIRATA, K., MORISHITA, A., HATTORI, M. & SAKAKURA, Y. 1990 Viscoelastic properties of middle ear effusions from pediatric otitis media with effusion and their relation to gross appearance. *Europ. Arch. Oto-Rhino-Laryngol.* **247** (1), 60–62.

WILLIAMSON, C. & GOVARDHAN, R. 2004 Vortex-induced vibrations. *Annu. Rev. Fluid Mech.* **36**, 413–455.

https://doi.org/10.1017/jfm.2017.15 Published online by Cambridge University Press